CHAPTER-6

Synthesis, characterization, and electrochemical evaluation of $CuMnSe_2$/ppy composite for alkaline water oxidation

6.1. Abstract

Hydrogen has garnered a lot of recognition for being clean and sustainable energy source, yet natural gas reformation presently provides the bulk of industrial hydrogen. The creation of effective, affordable, and durable electrocatalysts for the direct synthesis of hydrogen through water with little electrical input is a major goal in large-scale electrolysis. Using earth-abundant electrocatalysts to improve the water oxidation reaction, a critical step toward effective water splitting, is a potential strategy. In order to increase catalytic efficiency, Cu doped manganese diselenide ($CuMnSe_2$) was hydrothermally synthesized and coated onto the conductive polymer polypyrrole (ppy). When ppy was added, $CuMnSe_2$ produces a large number of active charge carriers that improved water oxidation reaction. The $CuMnSe_2$/ppy catalyst demonstrated impressive performance for the OER, showing an overpotential of 299 mV at a current density of 10 mA cm^{-2} (η_{10}), a Tafel slope of 91 mV dec^{-1}, and a charge transfer resistance of 16.76 Ω Rapid charge mobility to the polymer's surface was made possible by the effective charge transfer by the complete dispersion of ppy over $CuMnSe_2$ particles. The $CuMnSe_2$/ppy composite is shown in this study to be a very powerful catalyst with a great deal of promise for use in sustainable energy applications in the future.

6.2. Introduction

Research in hydrogen energy as a sustainable substitute has increased as a result of the worsening energy crisis [1,2]. An ecologically favorable technique for producing hydrogen, is electrochemical water splitting, which includes the evolution of hydrogen and the oxygen at the cathode and at the anode respectively [3,4]. The actual voltage which is known as overpotential, needed for water splitting, however, is more than the predicted thermodynamic

optimum of 1.23 V vs. RHE [5], that in turn leads to energy losses that lower the process's overall efficiency. Achieving effective total water splitting in a range of pH environments is further complicated by the different reaction mechanisms and conditions for HER and OER. The inherent electrocatalytic functionality and active site density of materials are the main determinants of their catalytic efficacy. By choosing the right materials and altering their surface and interface structures, catalytic activity may be increased [6]. Platinum (Pt) and ruthenium oxide (RuO_2), two traditional electrocatalysts for HER and OER, show outstanding output but have limited practical uses because of their high cost and unavailability. Non-noble metal-based electrocatalysts for water splitting have improved significantly in recent years, providing prospective substitutes for precious metals [7–9].

The four-electron transfer mechanism for alkaline water oxidation, which includes the formation of a dioxygen (O_2) molecule through a link between two oxygen atoms (O=O), is the main cause of its sluggish kinetics [10]. In order to replace the existing cutting-edge catalysts in alkaline water oxidation, there is an urgent need for electrode materials that are inexpensive, plentiful, and extremely effective. In order to overcome this obstacle, plenty of investigations has currently been done on creating long-lasting support structures and sophisticated electrode materials specifically for water-splitting applications. Numerous electrocatalysts have been studied as possible substitutes for HER and OER in recent years, including metal alloys, noble metals, transition metal oxides, metal-based materials (like carbides, nitrides, phosphides, and sulfides), chalcogenides, and composites [11].

Because of their remarkable electrocatalytic activity, catalysts based on transition metal chalcogenides (TMCs) have recently attracted an enormous amount of interest, outperforming conventional metal oxides and alloys [12–15]. This is especially noteworthy since metal-rich

chalcogenides' flexible stoichiometric tunability offers excellent efficiency, affordability, resilience, and the potential to be a good substitute for noble metals in the OER catalysis. The catalytic site's capacity to easily undergo electrochemical tuning with a low energy barrier is a crucial component in improving electrochemical performance. Materials based on manganese (Mn) are particularly noteworthy in this regard because of Mn's ease of adopting different oxidation states. Additionally, Mn-based compounds are very appealing for OER applications because to their inexpensive cost, less toxicity, and widespread natural availability. Even with these encouraging characteristics, research on Mn-based compounds as OER catalysts is noticeably lacking, and there aren't many papers showcasing its potential in this field [12,13].

Furthermore, by producing unbalanced Coulombic forces that encourage atomic rearrangement and the production of defects, metal doping can cause the formation of catalytic edges [16,17]. Through enhancing the quantity of active sites, these changes increase the electrocatalytic functionality of the OER and promote more effective electron transfer [18,19]. Additionally, it has been demonstrated that doping with transition metals increases the density of accessible catalytic sites, which enhances catalytic performance overall [20]. One of the most plentiful and reasonably priced metals is copper. Particularly, copper selenides have garnered interest because of their advantageous chemical and physical properties, that greatly accelerate the catalytic activity. They are interesting options for OER applications mostly owing to their superior electrical conductivity, which is substantially responsible for this enhancement [21,22].

Because of the exceptional stability, high conductivity, and plentiful nitrogen content, conducting polymers like polypyrrole (ppy) have become promising cocatalysts. When combined with transition metal-based materials, these polymers can form transition metal-N

coordinate bonds [23–25]. For instance, Yang *et al.* used a polypyrrole hydrogel incorporating cobalt and iron to develop an innovative trifunctional electrocatalyst for self-sustaining overall water splitting [26].

In this work, we investigate a composite material's electrochemical performance for OER applications. Inspired by the components' encouraging features, we created the Cu doped MnSe2/ppy hybrid composite utilizing a straightforward hydrothermal synthesis that followed solid state grinding. With a moderate Tafel slope of 91 mV dec^{-1}, an exceptionally less overpotential of 299 mV (η_{10}) for OER in an alkaline aqueous solution. The as-prepared hybrid material exhibits exceptional electrocatalytic efficiency.

6.3. Experimental

6.3.1. Materials

Se powder (AR, Merck, 99.9%), Copper Nitrate trihydrate ($Cu(NO_3)_2.3H_2O$) (AR, Merck, 99.9 %), Hydrazine hydrate ($N_2H_4.xH_2O$), Manganese Chloride hexahydrate ($MnCl_2 \cdot 6H_2O$) (AR, Merck, 99.9 %), and Pyrrole (AR, Merck, 99.9%).

6.3.2. Synthesis of $CuMnSe_2$

Hydrothermal synthesis was used to create $CuMnSe_2$. After completely dissolving 0.33 mmol of manganese chloride hexahydrate and 0.33 mmol of copper nitrate trihydrate in 20 mL of ultrapure Milli-Q water, the mixture was rapidly mixed for 15 minutes using a magnetic stirrer. After adding 0.11 g of selenium powder, the mixture was stirred for a further half hour. After that, a black precipitate formed when 10 mL of hydrazine hydrate ($N_2H_4 \cdot xH_2O$) was introduced by drops. After that, the solution was continuously mixed in a magnetic stirrer for two hours.

This mixture of precursors was then moved to a 50 mL hydrothermal autoclave lined with Teflon and applied at 180 °C for 12 hours in a hot-air oven. The hydrothermal autoclave was left to spontaneously cool down to achieve ambient temperature once the reaction was finished. After being properly cleaned many times with ethanol and distilled water, the precipitate was let to dry overnight at 45 °C.

6.3.3. Synthesis of polypyrrole

The pyrrole monomer was maintained in dark and in an inert environment during the procedure to avoid oxidation. To guarantee even dispersion, pyrrole monomer (0.4 mL), added in double distilled water (50 mL) is initially mixed together and gently shaken during the synthesis. 50 mL of anhydrous $FeCl_3$ aqueous solution was then introduced by drops to the continuously stirring solution while it was in a nitrogen environment. For six hours, the polymerization process was conducted at temperatures between 0 to 5 °C. After the reaction, the resultant polypyrrole was filtered and carefully cleaned using methanol and double-distilled water until the pH of the washings become 7. The final polypyrrole material was obtained by vacuum-drying the product for 12 hours at 60 °C.

6.3.4. Synthesis of $CuMnSe_2$/ppy composite

The composite was made using a solid-state synthesis technique. To guarantee complete mixing, an equal amount of $CuMnSe_2$ and polypyrrole were first mixed and grind together in a mortar for two to three hours. The resultant mixture was then ultrasonically treated for an hour in an ethanol solution to attain total homogeneity. To finish the preparation procedure, the composite was finally dried at 45 °C.

6.3.5. Preparation of working electrode

The working electrode's conductive substrate was fluorine-doped tin oxide (FTO). A mixture consisting of 40 μL of ethanol, 20 μL of double-distilled water, and 10 μL of 5 % Nafion was mixed with 1 milligram of the synthesized catalyst to formulate the catalyst ink. After that, the resulting mixture underwent ultrasonic treatment for about an hour to guarantee that the catalyst particles were distributed evenly. 20 μL of the resultant catalyst ink was gently dropped and cast over the FTO substrate after sonication, and it was then allowed to naturally dry at room temperature.

6.3.6. Electrode preparation for spectro-electrochemical study

The previously reported catalyst ink was utilized to make the working electrode for the *operando* spectro-electrochemical study. To guarantee adequate coating for use in the electrochemical measurements of the study, a platinum grid was first immersed in the catalyst ink and then allowed to dry at room temperature.

6.4. Characterizations

6.4.1. Physicochemical characterizations

Using a Rigaku Smart Lab 9 kW powder diffractometer set to 1.514 Å, powder X-ray diffraction (XRD) was implemented to examine the crystalline and amorphous phases of the produced catalysts. FE-SEM (Field emission-scanning electron microscopy) on a Nova Nano-SEM and HR-TEM (High resolution-transmission electron microscopy) on a Thermo Fisher Technai 20 G^2 were used to analyze the materials' morphological and microstructural characteristics. EDS (Energy dispersive spectroscopy) and elemental mapping were utilized to

further examine the distribution and content of the elements inside the catalysts, yielding important information about the material's composition.

6.4.2. Electrochemical characterizations

Three electrodes were used in a single-compartment Pyrex glass cell for the electrochemical studies. The working electrode was the FTO/catalyst electrode, which had a working surface area of 0.5 cm^2, and the counter electrode was an 8 cm^2 piece of platinum foil (Aldrich, 99.9% purity). Using a Hg/HgO/1 M KOH reference electrode, all potentials were compared to the standard electrode potential of Hg/HgO, which is 105.3 mV vs. NHE [27]. Utilizing a Luggin capillary salt bridge made with agar-agar and KCl, the electrolyte was connected to the reference electrode. A CHI-608C instrument (CH Instruments, USA) was used for electrochemical characterization, which included Tafel polarization measurements, electrochemical impedance spectroscopy (EIS), and cyclic voltammetry [28–30]. To relate potential values measured by the Hg/HgO reference electrode to the reversible hydrogen electrode (RHE), **Equation 3.1** could be used which is already discussed in **Chapter 3**.

$$E_{RHE} = E_{Hg/HgO} + 0.0592 \times pH + E^0_{Hg/HgO} \qquad \textbf{(3.1)}$$

6.4.3. Spectro-electrochemical characterizations

A platinum wire was used as the counter electrode for the spectro-electrochemical investigations, and a platinum grid covered with the catalyst ink was employed as the working electrode inside a quartz cuvette. A Hg/HgO electrode submerged in a 1 M KOH electrolyte served as the reference electrode. To provide robust electrochemical measurements, an agar-agar and KCl-made Luggin capillary salt bridge was implemented to link the reference

electrode to the electrolyte. Spectra were obtained during LSV at 5 mV s^{-1} scan rate, close to the onset potential. The Ocean Optics FLAME-T-XR1-ES assembly was used to perform *operando* spectro-electrochemical measurements spanning a wavelength range of 200 nm to 1025 nm.

6.5. Results and discussion

6.5.1. Physicochemical characterizations

6.5.1.1. XRD

Figure 6.1 displays the XRD patterns of polypyrrole (ppy), Cu doped $MnSe_2$ ($CuMnSe_2$), and ppy composite of Cu doped $MnSe_2$ ($CuMnSe_2$/ppy) samples. In the composite **(Figure 6.1 (c))** and $CuMnSe_2$ **(Figure 6.1 (b))** sample, distinct diffraction peaks were identified at 27.79°, 31.2°, 33.7°, 39.4°, and 49.6°, corresponding to the (200), (210), (211), (220), and (023) lattice planes of the cubic phase (JCPDS no. 89-3709) respectively. The peaks validate the cubic crystalline configuration. The XRD investigation further indicated the existence of secondary phases, including Cu_2Se and MnSe. The peaks at 27.47°, 44.8°, and 53.4° correspond to the (111), (220), and (311) reflections of the cubic Cu_2Se phase (JCPDS no. 01-088-2043) and the peaks at 32.8°, 47.1°, 55.7°, and 58.6° corresponds to (200), (220), (311), and (222) reflections of the cubic MnSe phase (JCPDS no. 00-011-0683) [31]. These extra peaks reveal the coexistence of Cu_2Se and MnSe in the prepared samples.

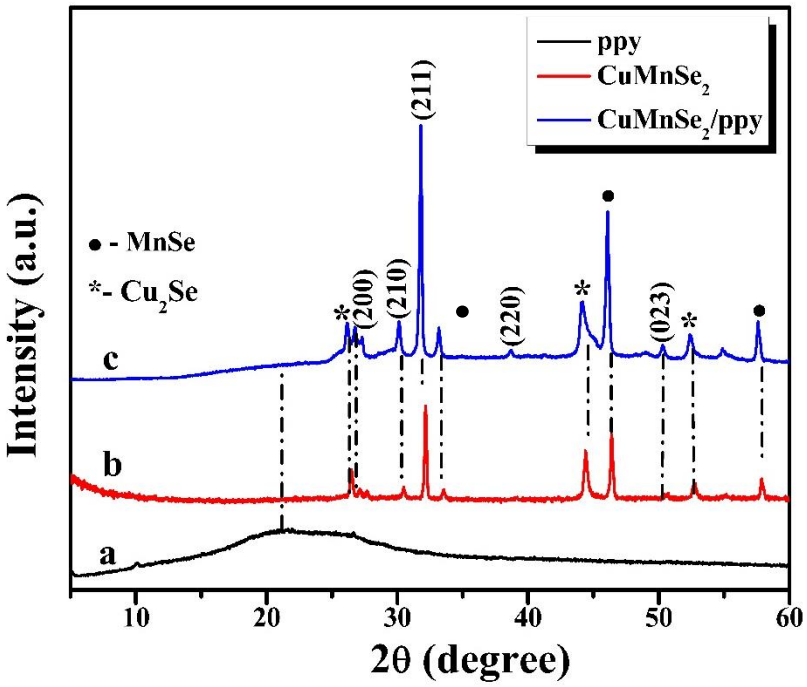

Figure 6.1. XRD patterns of **a)** ppy, **b)** $CuMnSe_2$, **c)** $CuMnSe_2$/ppy.

Further broad peak at low angles corresponds to amorphous nature of ppy as demonstrated in **Figure 6.1 (a)**. The inclusion of ppy does not impact the crystal lattice of the composite. This confirms that the polypyrrole is dispersed over the $CuMnSe_2$ material and not intercalated [32].

6.5.1.2. FE-SEM

The $CuMnSe_2$/ppy composite material is shown in FE-SEM images **(Figures 6.2 (a) and (b))** at different magnifications. The FE-SEM image shows a rod like structure with a layer of polypyrrole. Further, heterogeneous dispersion of smaller particles with different shapes are also present. These particles appear to aggregate and coalesce, forming larger structures, indicative of a growth mechanism that favors the clustering of smaller, irregularly shaped particles into more defined aggregates [33]. The stoichiometric character of the synthesized

catalyst is further supported by the EDS spectra acquired from FE-SEM, indicating that composite has with almost perfect elemental ratios. The elemental peaks in the EDS data are in line with the anticipated compositions confirming the existence of the elements. The EDS analysis **(Table 6.1)** and elemental mapping data, provided in **Figure 6.3** and **6.4** respectively, further support these findings.

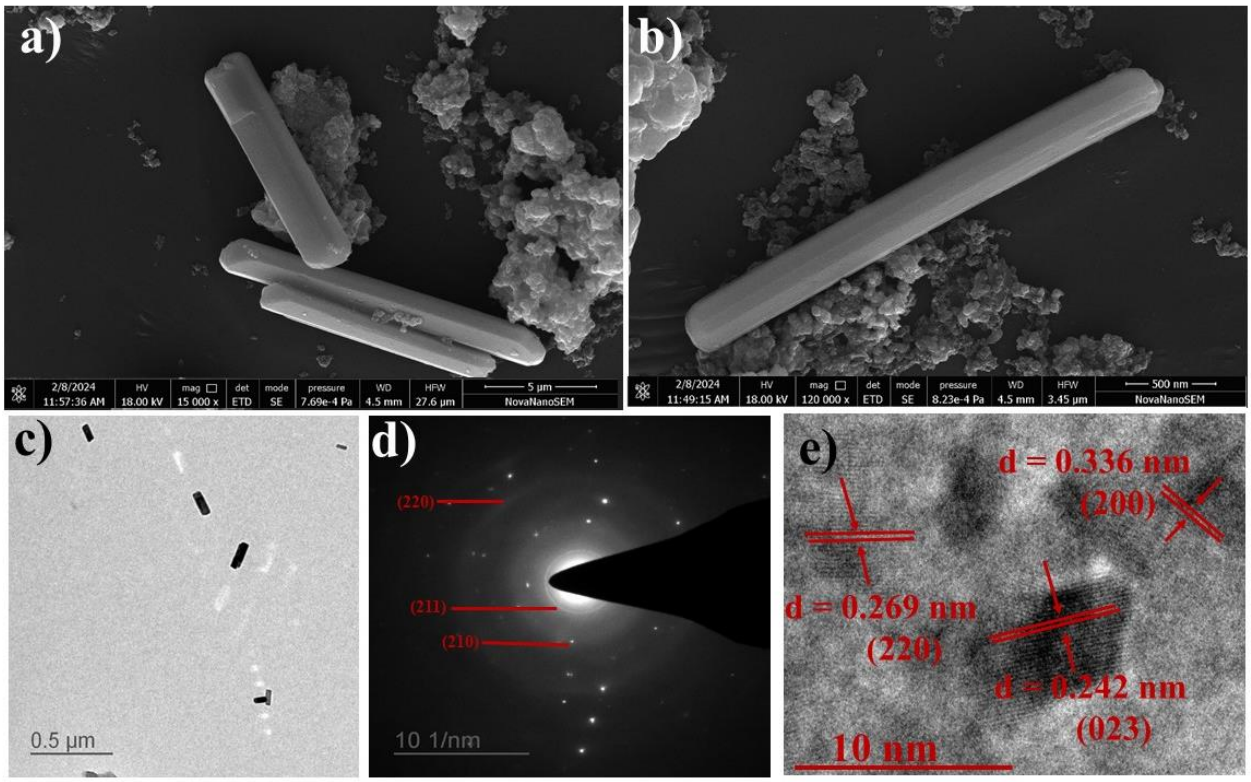

Figure 6.2. a, b) FE-SEM micrographs of $CuMnSe_2$/ppy at different magnifications, **c)** TEM micrograph of $CuMnSe_2$/ppy, **d)** SAED pattern, **e)** HR-TEM image of $CuMnSe_2$/ppy.

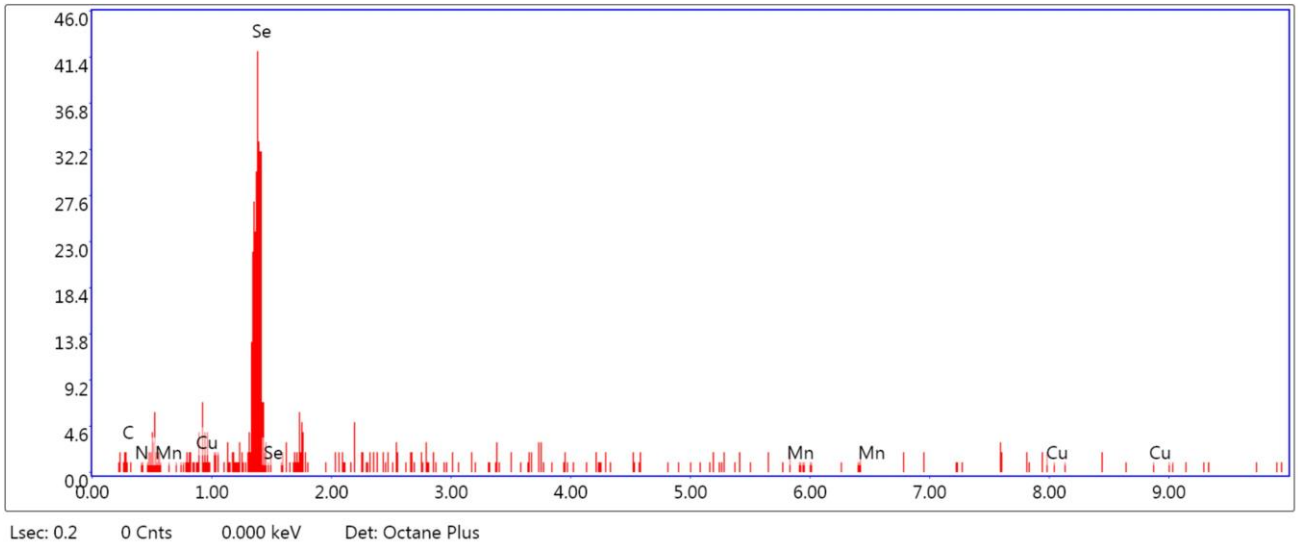

Figure 6.3. EDS spectra of composite ($CuMnSe_2$/ppy).

Table 6.1. Elemental composition from EDS spectra.

Element	Weight %	Atomic %	Net Int.	Error %	Kratio	Z	A	F
C K	11.46	38.50	88.30	39.67	0.0368	0.8775	0.3657	1.0000
N K	5.51	15.88	36.40	96.03	0.0180	0.8438	0.3872	1.0000
SeL	63.00	32.20	1199.50	11.38	0.3746	0.5568	1.0683	0.9996
MnK	7.10	5.21	58.70	86.67	0.0531	0.6980	1.0005	1.0718
CuK	12.93	8.21	51.30	88.18	0.1111	0.7729	1.0026	1.1091

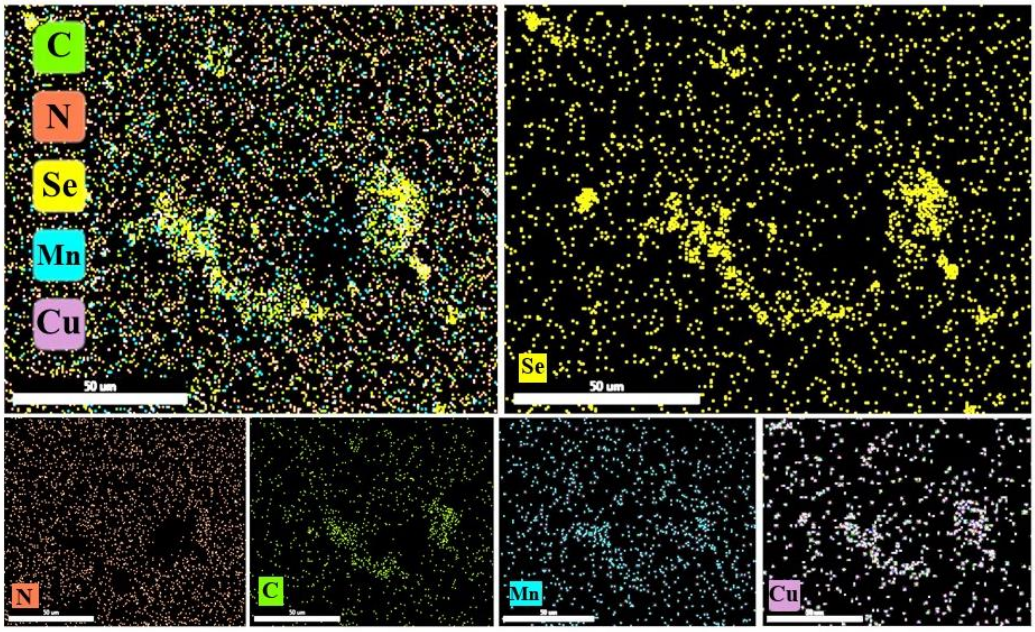

Figure 6.4. Elemental mapping.

6.5.1.3. HR-TEM

The distinctive microstructure of the $CuMnSe_2$/ppy composite, seen in **Figure 6.2 (c)**, was investigated using the TEM technique. The composite material's microstructure is similar to that of the SEM micrographs, but considerably smaller. This analysis confirms the particle size distribution of the synthesized material, which is not readily apparent in the SEM images due to the aggregation of particles. The SAED pattern of the composite material is shown in **Figure 6.2 (d)**. Three separate diffraction rings, which correspond to the (211), (210), and (220) crystallographic planes, agrees with the XRD data. Further, HR-TEM image of prepared catalyst **(Figure 6.2 (e))** shows distinct lattice fringes and the d spacing calculated from these fringes are well aligned with the respective planes which is already confirmed by the XRD patterns.

6.5.2. Electrochemical characterizations

6.5.2.1. OER study

The produced catalysts' electrochemical OER activity was assessed in alkaline electrolytes. **Figure 6.5** displays the related electrochemical data. **Figure 6.5 (a)** displays the LSV curves at 5 mV s^{-1} scan rate. The composite $CuMnSe_2$/ppy shows an overpotential of 286 mV (η_{10}), indicating effective charge transfer at the electrode/electrolyte interface than its individual constituents as clearly shown by **Figure 6.5 (c)**. This result demonstrates the catalytic potential of the produced catalyst and is competitive with numerous currently available OER catalysts.

The same material was put through 20 cycles of accelerated deterioration (AD) using CV testing to evaluate the catalyst's stability and longevity. A little rise in overpotential with prolonged cycling was shown by the overpotential measurement, which was 299 mV (η_{10}) post-AD. This little alteration confirms that the composite material continues to be electrochemically active and stable, underscoring the catalyst's resilience to repeated cycle conditions. These results highlight the synthesized material's potential performance and long-term stability for OER applications.

Apart from the apparent current density (j_{app}), the specific current density (j_{spec}) known for a measure of a current density normalized by the material loading, and true current density (j_{true}) that is a measure of current density, normalized by the electrode roughness factor, could be used to evaluate the OER catalytic activity. This normalizing technique helps to better understand the intrinsic electrochemical activity of the $CuMnSe_2$/ppy composite in promoting the oxygen evolution process (OER). By taking into consideration, factors like surface area and electrode loading, this approach guarantees a better comparison of catalytic functionality

among various catalysts and offers a more transparent evaluation of the inherent catalytic efficiency [34]. The produced catalysts' j_{spec}, j_{true}, and j_{app} are shown in **Table 6.2**, together with the overpotentials (η) that were computed at the designated current densities using **Equation 1.19 (**From **Chapter 1)**. Both j_{true} and j_{app} give a more accurate picture of the rate of alkaline water oxidation when the data is normalized using the oxide roughness factor or the geometric surface area of the electrode [34].

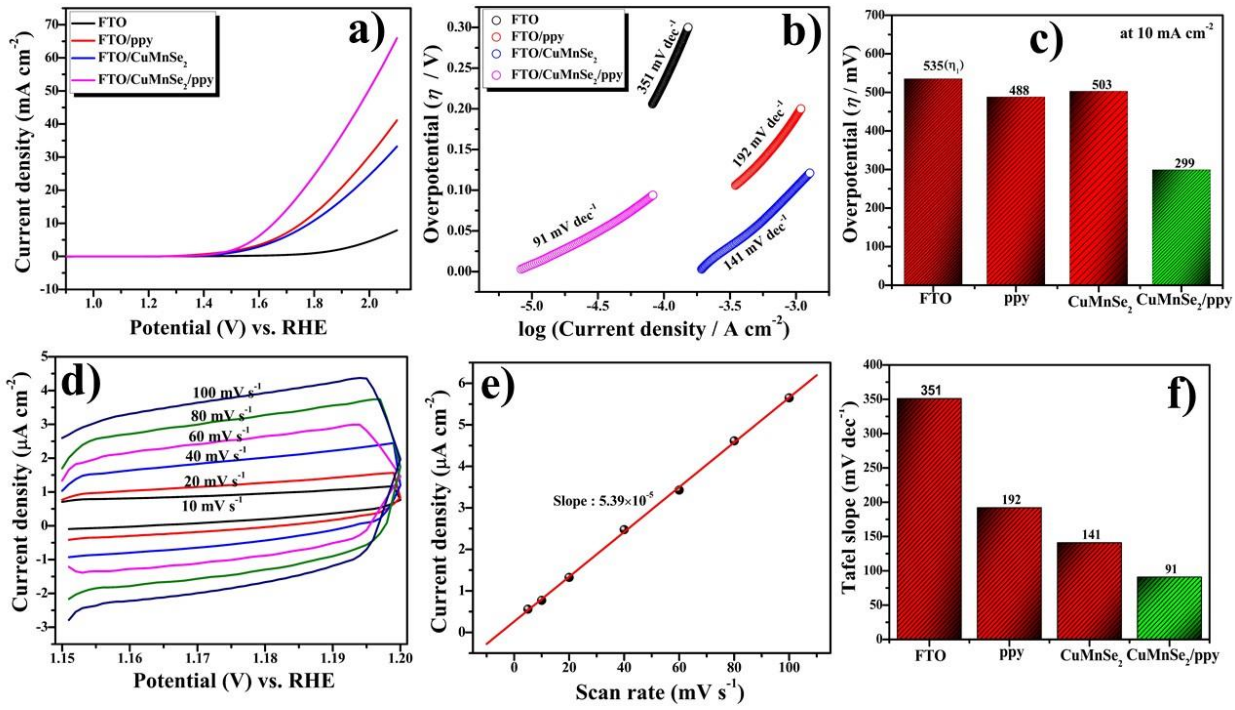

Figure 6.5. a) LSV overlay of prepared electrodes at 0.5 mV s^{-1} scan rate in 1 M KOH at room temperature, **b)** Tafel slopes, **c)** Overpotential variation with the prepared electrocatalysts and bare electrode, **d)** CV of FTO/$CuMnSe_2$/ppy electrode in non-faradaic region at varying scan rates, **e)** C_{dl} plot for FTO/$CuMnSe_2$/ppy electrode **f)** Tafel slope variation with the prepared catalysts and bare electrode.

The overpotential (η) for the FTO/$CuMnSe_2$/ppy catalyst is determined to be around 299 mV. Particularly when contrasted with more sophisticated catalysts like RuO_2, which has an overpotential of about 240 mV, these results show competitive efficiency. The functionality of the produced electrocatalysts is in line with that of cutting-edge materials, highlighting their potential effectiveness in accelerating the OER and establishing them as viable substitutes for traditional catalysts in energy conversion applications [35].

In this investigation, we also assessed the catalysts' roughness factor (R_f) and electrochemically active surface area (ECSA) which provide relevant information on the arrangement and distribution of the reactive intermediate sites on the electrode surface. The catalyst's surface shape is indicated by the roughness factor (R_f). An increased surface area that boosts the catalyst's adsorption ability and creates a more conducive environment for catalytic activity is indicated by a larger R_f value, greater than 1. The catalyst's performance in the OER may be greatly enhanced by this increased roughness. Optimizing catalyst design to improve electrochemical efficiency requires an understanding of these aspects [36].

Equation 1.22 (From **Chapter 1**) provided the proper way for calculating the ECSA. The $CuMnSe_2$/ppy composite outperforms the other catalysts with the maximum double-layer capacitance (C_{dl}) of 94.44 μF cm^{-2} and an ECSA of 1.18 cm^2, as seen in **Table 6.2**. This suggests that the composite material has a greater surface area that is electrochemically active, which is necessary to increase catalytic activity. The $CuMnSe_2$/ppy composite seems to have more exposure for intermediate active sites, which are essential for the electrolysis process, based on the higher ECSA value. The total catalytic effectiveness for OER is increased by these active sites, which enable effective electron-proton coupling between the electrode and the electrolyte [37].

Table 6.2. Kinetic parameters for prepared catalysts

Electrode	Overpotential (mV) at 10 mA cm^{-2}	Current density at E = 2V (mA cm^{-2})			C_{dl} (μF cm^{-2})	R_f	ECSA (cm^2)	Tafel Slope (mV dec^{-1})
		j_{app}	j_{true}	$j_{specific}$				
Bare	535 (η_1)	4.87	4.68	14.75	41.60	1.04	0.52	351
FTO/ppy	488	31.31	35.91	94.88	34.88	0.87	0.44	192
FTO/$CuMnSe_2$	503	25.83	10.94	78.27	26.97	0.67	0.34	141
FTO/$CuMnSe_2$/ppy	299	56.13	83.25	170.09	94.44	2.36	1.18	91

The double-layer capacitance (C_{dl}) has been estimated using CV in the non-faradaic region (1.15 V to 1.20 V vs. RHE) at various scan rates ranging from 20 mV s^{-1} to 100 mV s^{-1} **(Figure 6.5 (d))**. A linear connection was obtained by plotting the current density vs. scan rate **(Figure 6.5 (e))**. According to **Equation 1.23** (From **Chapter 1**), the slope of this linear plot was divided in half to get the C_{dl}. This technique allows for the exact measurement of the electrochemical double-layer capacitance, that is crucial for figuring out the catalysts' electroactive surface area [38].

The Tafel equation, $\eta = b \log j$, where b is the Tafel slope, j is the current density, and η is the overpotential was employed to calculate the Tafel slope, a crucial metric in assessing catalytic activity. By establishing a connection between the overpotential and the log current density, this equation offers important information on the OER kinetics and the overall efficacy of the catalysts. With lower values generally indicating quicker reaction kinetics and better catalytic effectiveness, the Tafel slope is especially helpful for examining the rate of electron transfer during the OER [39]. The $CuMnSe_2$/ppy composite had improved catalytic activity over its separate components, as seen in **Figure 6.5 (b)**, showing the least Tafel slope of 91 mV dec^{-1}.

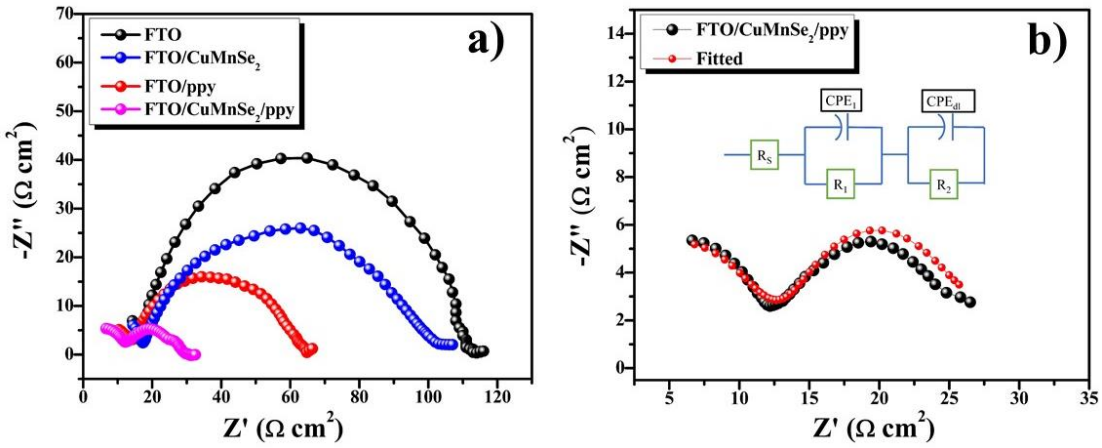

Figure 6.6. a) Nyquist plots at 1.45 V (vs. RHE), **b)** Fitted Nyquist plot of FTO/$CuMnSe_2$/ppy electrode.

One important metric for assessing the effectiveness of OER, is the charge transfer resistance (R_{ct}) at the electrode/electrolyte interface. The R_{ct} was monitored by Nyquist plots as shown in **Figure 6.4 (a)**. An equivalent circuit model was employed to explain the observed impedance spectra, a semi-circular form of the Nyquist plot in inset of **Figure 6.4 (b)**, in order

to better quantify and analyze the electrochemical behavior. The components that make up the equivalent circuit simulate the functioning of the electrode/electrolyte interface by modeling the solution resistance (R_s), the charge transfer resistance (R_{ct}), and the electrode film resistance (R_f). In the Nyquist plot, the charge transfer resistance (R_{ct}) is often shown as a semicircle, with the diameter of the semicircle representing the resistance at the electrode/electrolyte interface. Conversely, the curvature at the plot's origin represents the solution resistance. When comparing the $CuMnSe_2$/ppy composite to the separate $CuMnSe_2$ and ppy components, a smaller semicircle diameter is seen, suggesting a lower R_{ct} and quicker charge transfer processes. Since the reduced charge transfer resistance promotes more effective electron and ion movement throughout the process, this discovery highlights the composite's increased catalytic activity in OER [40]. The optimized pore structure of the composite, which raises the charge concentration close to the electrode surface, might be one reason for this improvement.

Table 6.3. Circuit parameters

Electrode	**Solution resistance (R_s) (Ω)**	**Electron transfer resistance (R_1) (Ω)**	**Charge transfer resistance (R_2) (Ω)**
Bare	4.99	13.35	99.14
FTO/ppy	7.81	8.65	50.70
FTO/$CuMnSe_2$	6.74	18.82	45.12
FTO/$CuMnSe_2$/ppy	4.61	15.12	16.76

The synergistic effects of the $CuMnSe_2$ and ppy components greatly increase overall charge transport efficiency and decrease interfacial resistance by lowering the charge transfer resistance (R_{ct}) at the electrode/electrolyte interface. These results demonstrate the $CuMnSe_2$/ppy composite's ability to support efficient electrochemical reactions, suggesting that it might be used as a material for energy conversion applications. **Table 6.3** offers further information on the electrochemical behavior and performance of the catalysts by providing additional circuit parameters for comparison. These metrics offers an improved overview of the electrochemical characteristics of the composite and aid in quantifying the contributions of various constituents to the overall catalytic efficiency.

6.5.2.2. Thermodynamic study

The standard thermodynamic parameters were measured. These included the standard electrochemical energy of activation ($\Delta H_{el}^{0\neq}$), the standard entropy of activation ($\Delta S^{o\neq}$), and the standard enthalpy of activation ($\Delta H^{o\neq}$). In order to maintain consistent conditions throughout the experiment, the reference electrode was allowed to remain at a steady temperature of 25 °C. Anodic polarization curves were recorded in a 1 M KOH electrolyte throughout a temperature span of 25 °C to 55 °C **(Figure 6.7 (a))**. The temperature dependency of the electrochemical reaction rates was examined using the Arrhenius plots **(Figure 6.7 (b))**. The activation energies for the various materials under study were taken from these plots and compiled in **Table 6.4**. The FTO/$CuMnSe_2$/ppy composite showed the lowest electrochemical activation energy among the electrodes evaluated, suggesting that the composite catalyst needs the least amount of energy to drive the reaction in comparison to the other materials. This

implies that with less energy input, the $CuMnSe_2$/ppy composite enhances the OER and enables more effective charge transfer.

The $CuMnSe_2$/ppy composite's average transfer coefficient (α) was found to be around 0.7, indicating effective electron transport. The formula $\alpha = 2.303\frac{RT}{bF}$, was used to get the transfer coefficient. Where T is the absolute temperature, R is the gas constant, F is the Faraday constant, and b is the Tafel slope. The average values of the thermodynamic parameters determined by using well-known equations **(Equations 1.27** and **1.29** From **Chapter 1)** are shown in **Table 6.4**. Polarization curves taken at varying temperatures were employed to calculate the Tafel slope (b, in mV dec^{-1}), that offers information on the kinetics of the process. The Boltzmann constant (k_B) and Planck's constant (h), which are essential for characterizing the system's thermodynamic behavior, were also included to the frequency component in the computations.

The FTO/$CuMnSe_2$/ppy electrode shows the greatest rate of adsorption among the materials studied, according to the electrochemical results. This suggests that the composite offers more active sites for reactive species adsorption. The higher catalytic activity reflects this improved adsorption capacity, which is in line with the thermodynamic data that has been obtained, especially the most negative value of the standard entropy of activation ($\Delta S^{o\neq}$), as seen in **Table 6.4**. An environment that is more favourable to the adsorption and subsequent electrochemical response of the OER is suggested by a higher negative $\Delta S^{o\neq}$.

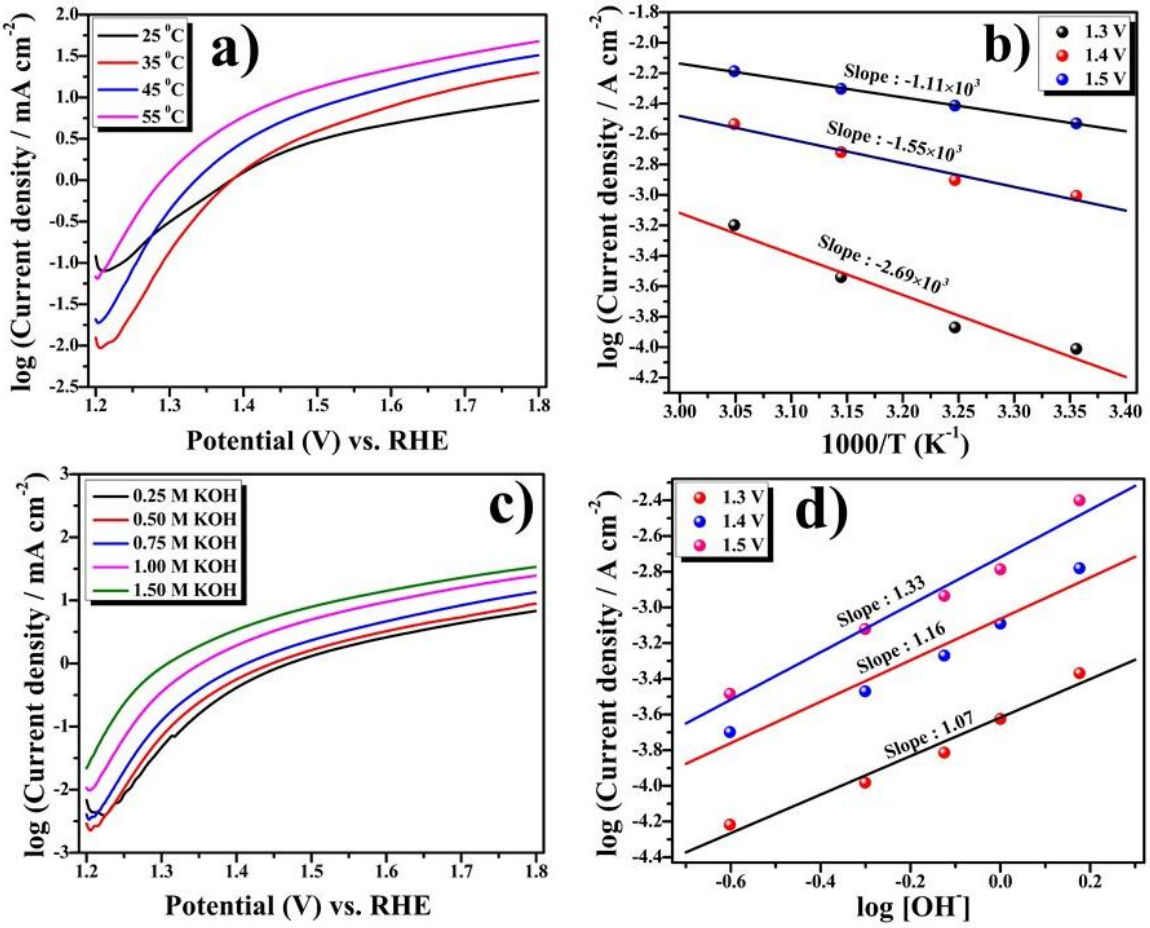

Figure 6.7. a) Tafel polarization plots of FTO/$CuMnSe_2$/ppy electrode at varying temperatures, **b)** Arrhenius plot, **c)** Tafel polarization plots of FTO/$CuMnSe_2$/ppy electrode at varying concentrations of KOH **d)** reaction order.

Table 6.4. Thermodynamic parameters

Electrode	Standard electrochemical energy of activation ($\Delta H_{el}^{0\neq}$) (kJ mol^{-1})	Standard electrochemical entropy of activation ($-\Delta S_{el}^{0\neq}$) (J K^{-1}mol^{-1})	Transfer coefficient (α)	Standard enthalpy of activation ($\Delta H^{0\neq}$) (kJ mol^{-1})
Bare	47.90	67.97	0.17	80.71
FTO/ppy	50.28	42.31	0.31	110.11
FTO/$CuMnSe_2$	31.64	109.71	0.42	112.70
FTO/$CuMnSe_2$/ppy	21.27	129.82	0.65	146.72

All the plots and measurements made for $CuMnSe_2$ catalyst are given below in **Figure 6.8.**

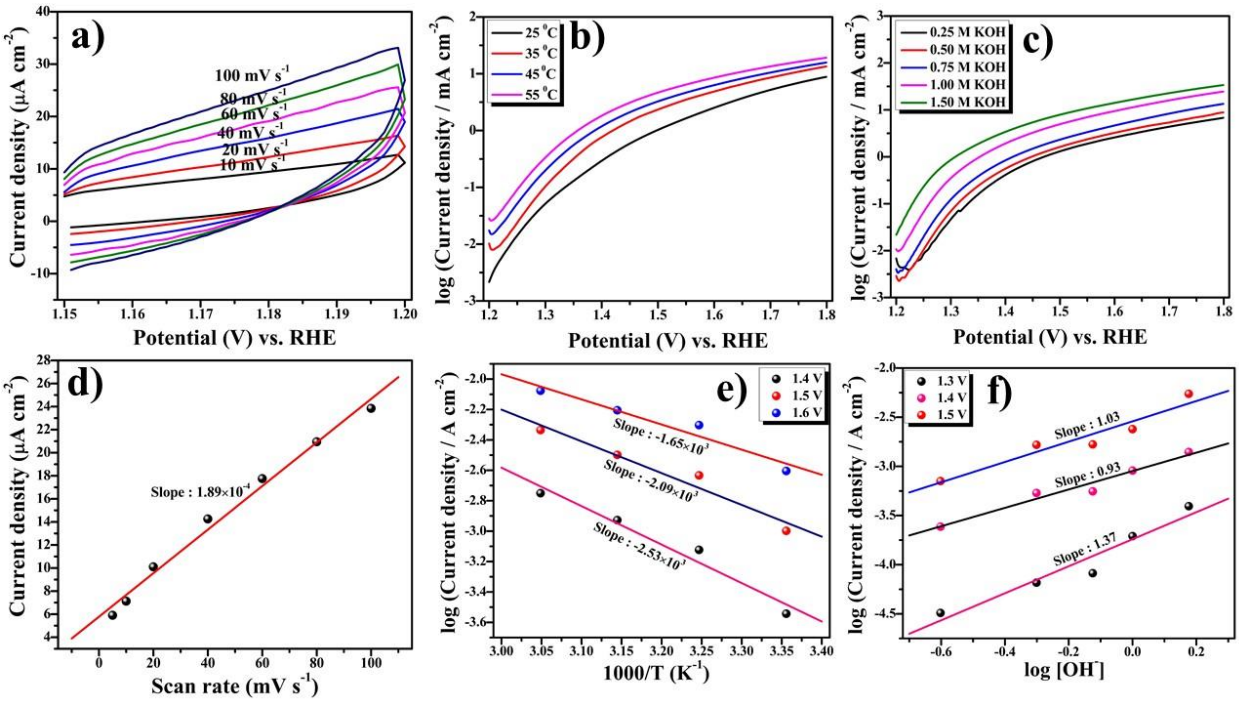

Figure 6.8. a) CV of FTO/$CuMnSe_2$ electrode in non-faradaic region at different scan rates, **b)** Tafel polarization curves of FTO/$CuMnSe_2$ electrode at different temperatures, **c)** Tafel polarization curves of FTO/$CuMnSe_2$ electrode at different concentrations of KOH, **d)** Corresponding C_{dl} plot for FTO/$CuMnSe_2$ electrode, **e)** Corresponding Arrhenius plot for FTO/$CuMnSe_2$ electrode, **f)** order of reaction for FTO/$CuMnSe_2$ electrode.

6.5.2.3. OER mechanism

Using previously published methods, the concentration of OH^- ions was varied to inspect the order of the alkaline water oxidation reaction [41]. Numerous investigations have shown that the observed non-integer reaction orders for each catalyst are not unusual [42,43]. This behavior is often ascribed to complicated reaction kinetics, in which the electrochemical process may include many steps or intermediates. These non-integer values indicate that the

OER mechanism is more complex than a straightforward first-order reaction, underscoring the need of more study to completely comprehend the catalytic dynamics.

The adsorption and ionization of OH^- ions on surface hydroxyl groups might be a potential cause for the observed non-integer reaction orders. In particular, the observed non-integer behavior might be impacted through the interaction between hydroxide ions and surface species, that could alter the reaction kinetics. The production and reactivity of surface hydroxyl groups during the electrocatalytic process may have a substantial effect on the adsorption energies and the stability of intermediate species in the OER. These surface interactions are important because they have the potential to impact reactive species adsorption and desorption, which in turn may impact the overall kinetics of OER. The significance of understanding how surface chemistry affects catalytic efficiency is highlighted by such intricate interactions [44].

Moreover, the coverage of adsorption intermediates, especially oxygen-containing species, which are created during the electrochemical development of molecular oxygen, might have a significant impact on the reaction kinetics. A linear connection between the adsorption energy and the extent of surface covering characterizes the interaction between these species and the catalyst surface under Temkin adsorption conditions. This implies that the energy required for further adsorption varies with the number of intermediates adsorbed, which has a direct impact on the OER rate. Therefore, when assessing the performance of electrocatalysts, surface coverage effects must be taken into consideration since they are essential to catalytic activity and efficiency [45,46].

Using a neutral KNO_3 electrolyte to ensure constant ionic strength, Tafel polarization curves **(Figure 6.7 (c))** were acquired for each manufactured electrode to better understand the chemical sequence involved in the OER. After analyzing polarization graphs acquired at

various KOH concentrations, linear log (current density) vs. log [OH^-] plots were produced **(Figure 6.7 (d))**. By computing the slopes of the linear sections from these curves, the reaction order was ascertained, providing more information about the order of electrochemical reactions.

In basic solution, the OER usually consists of four electrochemical stages (AEM). The proton transfer, one of the crucial phases in the OER process, is one of these steps. Following the adsorption and desorption of OH^- ions at the electrode's active sites **(Equation (4.1))**, a series of intermediate species (OH*, O*, OOH*, and OO*) are adsorbed on the metal surface to form oxygen-oxygen (O–O) bonds **(Equations (4.2), (4.3), and (4.4))** (Discussed in **Chapter 1**):

$$OH^- + M \rightarrow M + OH^* + e^- \quad \textbf{(4.1)}$$

$$OH^* + OH^- \rightarrow O^* + H_2O + e^- \quad \textbf{(4.2)}$$

$$OH^- + O^* \rightarrow OOH^* + e^- \quad \textbf{(4.3)}$$

$$OH^- + OOH^* \rightarrow O_2 + H_2O + e^- \quad \textbf{(4.4)}$$

The Bockris electrochemical mechanism for the OER is compatible with this route [45]. It is crucial to recognize that other reaction routes, such the Bockris-Otagawa peroxide route and those suggested by Krasil'shchikov, could potentially be involved [45]. The metal sites (designated as "M," such as Mn and Cu) are the active catalytic sites in this model, whereas the surface-adsorbed intermediates participating in the reaction are represented by OH* and O*.

6.5.2.4. Stability and durability

A catalyst must have both exceptional electrocatalytic functionality and long-term stability during extended usage in order to be deemed practically and economically feasible. Consequently, one of the most important aspects of evaluating an electrocatalyst is determining its stability and endurance. In this work, chronopotentiometry tests in a 1 M KOH electrolyte were utilized to investigate the stability of the FTO/$CuMnSe_2$/ppy electrode. The FTO/$CuMnSe_2$/ppy electrode exhibited remarkable stability over a 12-hour period, as seen in **Figure 6.9**, with no discernible change in its potential. This consistent performance during continuous operation shows that the electrode can maintain its catalytic activity without suffering appreciable degradation, even when gas bubbles evolve.

Any electrocatalyst must have this kind of resilience as it guarantees that the catalyst will continue to function well even after prolonged usage. The FTO/$CuMnSe_2$/ppy composite's exceptional stability underscores its promise for practical energy conversion devices like fuel cells and electrolyzers, where long-term performance is crucial. This outcome highlights the composite's applicability for commercial and industrial-scale operations where stability and high efficiency are necessary.

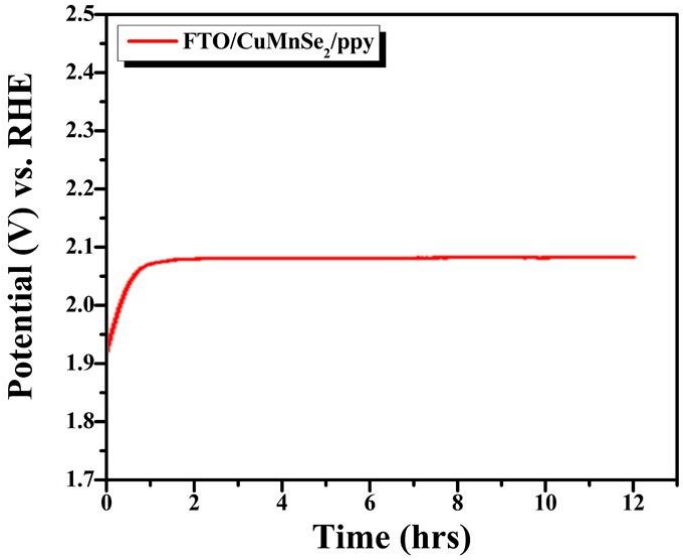

Figure 6.9. Chronopotentiometry test at 10 mA cm^{-2}.

6.5.3. *Operando* Spectro-electrochemical study

Both absorbance and the current passing through the electrochemical circuit are concurrently measured in UV-Vis spectro-electrochemistry (SEC). With this method, variations in the electrolyte environment, the applied voltage, and the ensuing optical and current responses may all be directly correlated. Although UV-Vis SEC is often used to investigate molecular systems, it may also be used to analyze electrode materials, providing important details on the electrocatalysis taking place on the facade of electrode. For watching changes in absorbance that are directly linked to electrochemical processes at the electrode interface, this approach is often used in a three-electrode cell arrangement, which permits fine control of the voltage delivered to the working electrode [47].

When performing LSV at room temperature in a 1 M KOH electrolyte at 5 mV s^{-1} scan rate, the *operando* UV-Vis spectroscopy data for the FTO/$CuMnSe_2$/ppy electrode are shown in **Figure 6.10**. A smaller peak is seen between 850 and 900 nm, and the absorbance spectra

show many different absorption peaks in the 300–440 nm region. As the electrode potential was gradually raised in steps of 0.1 V from 1.5 V to 2.1 V vs. RHE, these measurements were taken. Interestingly, the absorbance spectra widened and intensified with increasing applied voltage. The production of MnOOH species, a crucial step in the oxygen evolution process (OER), is probably indicated by these spectrum alterations. Its function in the catalytic process during OER is confirmed by the increase and intensity of these absorbance peaks, which indicate that the electrode surface's electrochemical activation is aiding in the synthesis of MnOOH [48].

By demonstrating how the material properties of the electrode change in response to applied potential and enabling a better comprehension of the intermediate species involved in the reaction, these *operando* UV-Vis spectroscopy results offer important insight into the dynamic changes occurring on the facade of the electrode while alkaline water oxidation.

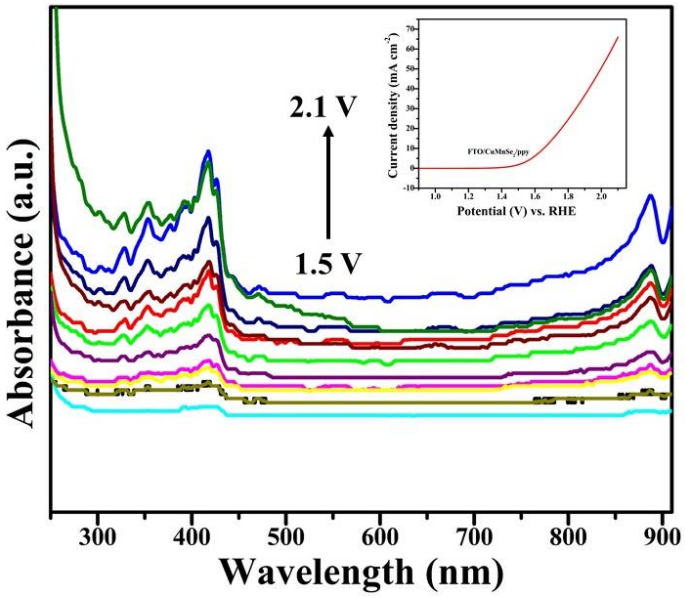

Figure 6.10. *Operando* UV-vis spectra of FTO/$CuMnSe_2$/ppy operating at 5 mV s^{-1} scan rate during LSV.

6.6. Conclusion

The $CuMnSe_2$/ppy composite's catalytic effectiveness for oxidizing alkaline water was carefully assessed. According to experimental results, a hydrothermal method which followed solid-state grinding may be used to produce $CuMnSe_2$/ppy effectively and economically. The FTO/$CuMnSe_2$/ppy electrode had the lowest Tafel slope among the other catalysts evaluated, indicating improved electrocatalytic functionality for alkaline water oxidation.

In comparison to the other materials evaluated, the catalyst elucidated the least standard electrochemical activation energy, that further confirms $CuMnSe_2$/ppy's remarkable performance. This implies that $CuMnSe_2$/ppy is more efficient overall because it needs less energy to drive the reaction. *Operando* spectro-electrochemical investigation showed that the MnOOH intermediate species, which are essential to the OER process, formed distinct absorption peaks in the 300–440 nm area. These results provide a better understanding of the catalyst's activity during electrochemical activation in addition to highlighting the reactive intermediate sites involved in the process. Furthermore, the production of different redox-intermediate active species during OER is suggested by the significant increase in electrocatalytic activity in $CuMnSe_2$/ppy, as seen by its peak absorbance intensity. These species are essential to the catalyst's exceptional performance, highlighting $CuMnSe_2$/ppy's potency as an OER catalyst.

Furthermore, $CuMnSe_2$/ppy's encouraging findings point to potential uses beyond water oxidation, especially in energy storage devices and other electrochemical applications. $CuMnSe_2$/ppy may be a crucial component for industrial-scale water splitting because to its excellent performance and stability, offering a sustainable and efficient means of producing renewable hydrogen fuel to satisfy the world's expanding energy needs. To completely

comprehend the function of such redox-intermediate active sites and improve the catalyst for large-scale applications, further research is required, particularly in the near-infrared (NIR) region.

6.7. References

[1] Y. Yuan, C. Han, L. Guo, X. Wu, Y. Zhao, Exploring the mechanisms of magnetic fields in supercapacitors: material classification, material nanostructures, and electrochemical properties, J. Mater. Chem. A 12 (2024) 6165–6189. https://doi.org/10.1039/d3ta07658j.

[2] W. Zhao, Y. Zeng, Y. Zhao, X.W.-J. of E. Storage, undefined 2023, Recent advances in metal-organic framework-based electrode materials for supercapacitors: A review, Elsevier (n.d.). https://www.sciencedirect.com/science/article/pii/S2352152X23003316 (accessed November 7, 2024).

[3] M. Zubair, I. Ihsanullah, H. Abdul Aziz, M. Azmier Ahmad, M.A. Al-Harthi, Sustainable wastewater treatment by biochar/layered double hydroxide composites: Progress, challenges, and outlook, Bioresour. Technol. 319 (2021). https://doi.org/10.1016/j.biortech.2020.124128.

[4] L. Lu, Y. Zheng, R. Yang, A. Kakimov, X. Li, Recent advances of layered double hydroxides–based bifunctional electrocatalysts for ORR and OER, Mater. Today Chem. 21 (2021). https://doi.org/10.1016/j.mtchem.2021.100488.

[5] Y. Zhao, Y. Wang, Y. Dong, C. Carlos, J. Li, Z. Zhang, T. Li, Y. Shao, S. Yan, L. Gu, J. Wang, X. Wang, Quasi-Two-Dimensional Earth-Abundant Bimetallic Electrocatalysts for Oxygen Evolution Reactions, ACS Energy Lett. 6 (2021) 3367–3375. https://doi.org/10.1021/acsenergylett.1c01302.

[6] N.T. Suen, S.F. Hung, Q. Quan, N. Zhang, Y.J. Xu, H.M. Chen, Electrocatalysis for the oxygen evolution reaction: Recent development and future perspectives, Chem. Soc. Rev. 46 (2017) 337–365. https://doi.org/10.1039/c6cs00328a.

[7] H. Sun, X. Xu, H. Kim, W.C. Jung, W. Zhou, Z. Shao, Electrochemical Water Splitting: Bridging the Gaps Between Fundamental Research and Industrial Applications, Energy Environ. Mater. 6 (2023). https://doi.org/10.1002/eem2.12441.

[8] F. Dionigi, J. Zhu, Z. Zeng, T. Merzdorf, H. Sarodnik, M. Gliech, L. Pan, W. Li, J. Greeley, P. Strasser, Intrinsic Electrocatalytic Activity for Oxygen Evolution of Crystalline 3d-Transition Metal Layered Double Hydroxides, Angew. Chemie 133 (2021) 14567–14578. https://doi.org/10.1002/ange.202100631.

[9] C. Han, Y. Zhao, Y. Yuan, Z. Guo, G. Chen, J. Yang, Q. Bao, L. Guo, C. Chen, Transition metal-based layered double hydroxides and their derivatives for efficient oxygen evolution reaction, Int. J. Hydrogen Energy 63 (2024) 918–936. https://doi.org/10.1016/j.ijhydene.2024.03.150.

[10] S.B. Roy, E. Jung, K.H. Kim, A. Patil, S.H. Chun, J.H. Park, S.C. Jun, Simultaneous integration of low-level rhenium (Re) doping and nitrogen-functionalized 3D carbon backbone into nickel-iron hydroxide (NiFeOH) to amplify alkaline water electrolysis at high current densities, Chem. Eng. J. 435 (2022).

https://doi.org/10.1016/j.cej.2022.135184.

[11] D. Duan, J. Gao, Y. Wang, X. Zhou, … S.L.-J. of E., undefined 2023, Electrodeposition of copper-cobalt bimetallic phosphide on nickel foam as an efficient catalyst for overall water splitting, Elsevier (n.d.). https://www.sciencedirect.com/science/article/pii/S1572665723003387 (accessed November 7, 2024).

[12] G. Mei, H. Liang, B. Wei, H. Shi, F. Ming, X. Xu, Z. Wang, Bimetallic MnCo selenide yolk shell structures for efficient overall water splitting, Electrochim. Acta 290 (2018) 82–89. https://doi.org/10.1016/j.electacta.2018.09.062.

[13] M. Sun, R.T. Gao, X. Liu, R. Gao, L. Wang, Manganese-based oxygen evolution catalysts boosting stable solar-driven water splitting: MnSe as an intermetallic phase, J. Mater. Chem. A 8 (2020) 25298–25305. https://doi.org/10.1039/d0ta09946e.

[14] W. Zhong, B. Xiao, Z. Lin, Z. Wang, L. Huang, S. Shen, Q. Zhang, L. Gu, RhSe2: A Superior 3D Electrocatalyst with Multiple Active Facets for Hydrogen Evolution Reaction in Both Acid and Alkaline Solutions, Adv. Mater. 33 (2021) 2007894. https://doi.org/10.1002/adma.202007894.

[15] X. Cao, E. Johnson, M. Nath, Identifying high-efficiency oxygen evolution electrocatalysts from Co-Ni-Cu based selenides through combinatorial electrodeposition, J. Mater. Chem. A 7 (2019) 9877–9889. https://doi.org/10.1039/c9ta00863b.

[16] X. Chen, Y. Qiu, G. Liu, W. Zheng, W. Feng, F. Gao, W. Cao, Y. Fu, W. Hu, P. Hu, Tuning electrochemical catalytic activity of defective 2D terrace MoSe2 heterogeneous catalyst: Via cobalt doping, J. Mater. Chem. A 5 (2017) 11357–11363. https://doi.org/10.1039/c7ta02327h.

[17] T. Tian, H. Gao, X. Zhou, L. Zheng, J. Wu, K. Li, Y. Ding, Study of the Active Sites in Porous Nickel Oxide Nanosheets by Manganese Modulation for Enhanced Oxygen Evolution Catalysis, ACS Energy Lett. 3 (2018) 2150–2158. https://doi.org/10.1021/acsenergylett.8b01206.

[18] L. Lin, N. Miao, Y. Wen, S. Zhang, P. Ghosez, Z. Sun, D.A. Allwood, Sulfur-Depleted Monolayered Molybdenum Disulfide Nanocrystals for Superelectrochemical Hydrogen Evolution Reaction, ACS Nano 10 (2016) 8929–8937. https://doi.org/10.1021/acsnano.6b04904.

[19] Y. Liu, X. Hua, C. Xiao, T. Zhou, P. Huang, Z. Guo, B. Pan, Y. Xie, Heterogeneous Spin States in Ultrathin Nanosheets Induce Subtle Lattice Distortion to Trigger Efficient Hydrogen Evolution, J. Am. Chem. Soc. 138 (2016) 5087–5092. https://doi.org/10.1021/jacs.6b00858.

[20] A.A. Tedstone, D.J. Lewis, P. O'Brien, Synthesis, Properties, and Applications of Transition Metal-Doped Layered Transition Metal Dichalcogenides, Chem. Mater. 28 (2016) 1965–1974. https://doi.org/10.1021/acs.chemmater.6b00430.

[21] R. Seoudi, A.A. Shabaka, M.M. Elokr, A. Sobhi, Optical properties and electrical conductivity studies of copper selenide nanoparticle, Mater. Lett. 61 (2007) 3451–3455. https://doi.org/10.1016/j.matlet.2006.11.087.

[22] F.F. Jaldurgam, Z. Ahmad, F. Touati, A. Al Ashraf, A. Shakoor, J. Bhadra, N.J. Al-Thani, T. Altahtamouni, Enhancement of thermoelectric properties of low-toxic and earth-abundant copper selenide thermoelectric material by microwave annealing, J. Alloys Compd. 904 (2022). https://doi.org/10.1016/j.jallcom.2022.164131.

[23] Q. Hu, G. Li, X. Liu, B. Zhu, X. Chai, Q. Zhang, J. Liu, C. He, Superhydrophilic Phytic-Acid-Doped Conductive Hydrogels as Metal-Free and Binder-Free Electrocatalysts for Efficient Water Oxidation, Angew. Chemie 131 (2019) 4362–4366. https://doi.org/10.1002/ange.201900109.

[24] M. Khalid, A.M.B. Honorato, H. Varela, L. Dai, Multifunctional electrocatalysts derived from conducting polymer and metal organic framework complexes, Nano Energy 45 (2018) 127–135. https://doi.org/10.1016/j.nanoen.2017.12.045.

[25] S. Dutta, A. Indra, Y. Feng, H.S. Han, T. Song, Promoting electrocatalytic overall water splitting with nanohybrid of transition metal nitride-oxynitride, Appl. Catal. B Environ. 241 (2019) 521–527. https://doi.org/10.1016/j.apcatb.2018.09.061.

[26] J. Yang, X. Wang, B. Li, L. Ma, L. Shi, Y. Xiong, H. Xu, Novel Iron/Cobalt-Containing Polypyrrole Hydrogel-Derived Trifunctional Electrocatalyst for Self-Powered Overall Water Splitting, Adv. Funct. Mater. 27 (2017). https://doi.org/10.1002/adfm.201606497.

[27] K. Kawashima, R.A. Márquez, Y.J. Son, C. Guo, R.R. Vaidyula, L.A. Smith, C.E. Chukwuneke, C.B. Mullins, Accurate Potentials of Hg/HgO Electrodes: Practical Parameters for Reporting Alkaline Water Electrolysis Overpotentials, ACS Catal. 13 (2023) 1893–1898. https://doi.org/10.1021/acscatal.2c05655.

[28] J.L.H. Chau, M.K. Hsu, C.C. Kao, Microwave plasma synthesis of Co and SiC-coated Co nanopowders, Mater. Lett. 60 (2006) 947–951. https://doi.org/10.1016/j.matlet.2005.10.054.

[29] R.N. Singh, J.P. Pandey, N.K. Singh, B. Lal, P. Chartier, J.F. Koenig, Sol-gel derived spinel MxCo3-xO4 (M = Ni, Cu; $0 \leq x \leq 1$) films and oxygen evolution, Electrochim. Acta 45 (2000) 1911–1919. https://doi.org/10.1016/S0013-4686(99)00413-2.

[30] R.N. Singh, J.P. Singh, B. Lal, M.J.K. Thomas, S. Bera, New NiFe2-xCrxO4 spinel films for O2 evolution in alkaline solutions, Electrochim. Acta 51 (2006) 5515–5523. https://doi.org/10.1016/j.electacta.2006.02.028.

[31] S. Nithiananth, K. Silambarasan, T. Logu, S. Harish, R. Ramesh, C. Muthamizhchelvan, M. Shimomura, J. Archana, M. Navaneethan, Transition divalent metal substitution in chalcopyrite CuInSe2 (In = Co, Ni, and Mn) counter electrode for dye-sensitized solar cell applications, Mater. Lett. 308 (2022) 130887. https://doi.org/10.1016/j.matlet.2021.130887.

[32] R. Bissessur, P.K.Y. Liu, S.F. Scully, Intercalation of polypyrrole into graphite oxide, Synth. Met. 156 (2006) 1023–1027. https://doi.org/10.1016/j.synthmet.2006.06.024.

[33] B.M. Palve, V.S. Kadam, C. V. Jagtap, S.R. Jadkar, H.M. Pathan, A simple chemical route to synthesis the CuSe and CuS counter electrodes for titanium oxide based quantum dot solar cells, J. Mater. Sci. Mater. Electron. 28 (2017) 14394–14401. https://doi.org/10.1007/s10854-017-7300-0.

[34] A.S. Chaddha, N.K. Singh, M. Malviya, A. Sharma, Birnessite-clay mineral couple in the rock varnish: a nature's electrocatalyst, Sustain. Energy Fuels 6 (2022) 2553–2569. https://doi.org/10.1039/d2se00185c.

[35] S. Pal, U.P. Azad, A.K. Singh, D. Kumar, R. Prakash, Studies on some spinel oxides based electrocatalysts for oxygen evolution and capacitive applications, Electrochim. Acta 320 (2019) 134584. https://doi.org/10.1016/j.electacta.2019.134584.

[36] A. Hojatshamami, Ni-Co and Ni-Fe Catalysts for The Oxygen Evolution Reaction in Alkaline Water Electrolysis, (2022). https://hdl.handle.net/11250/3042808 (accessed June 23, 2024).

[37] H. Zeng, Y. Zeng, J. Qi, L. Gu, E. Hong, R. Si, C. Yang, The role of proton dynamics on the catalyst-electrolyte interface in the oxygen evolution reaction, Chinese J. Catal. 43 (2022) 139–147. https://doi.org/10.1016/S1872-2067(21)63909-8.

[38] U.J. Awan, M.A. Basit, S.I.A. Shah, J. Yong-Xin, H. Zhifu, Minimized OER overpotential via SILAR-based development of g-C3N4/CdS nanocomposite, Appl. Phys. A Mater. Sci. Process. 129 (2023) 1–15. https://doi.org/10.1007/s00339-023-07105-y.

[39] Z. Hu, L. Hao, F. Quan, R. Guo, Recent developments of Co3O4-based materials as catalysts for the oxygen evolution reaction, Catal. Sci. Technol. 12 (2022) 436–461. https://doi.org/10.1039/d1cy01688a.

[40] A. Bard, L. Faulkner, H. White, Electrochemical methods: fundamentals and applications, 2022. https://books.google.com/books?hl=en&lr=&id=Sct6EAAAQBAJ&oi=fnd&pg=PR21&ots=QV3mtaJ0NX&sig=DLfrR_jFcE_cWnGqn5_EbKOHFu0 (accessed May 6, 2024).

[41] R.N. Singh, N.K. Singh, J.P. Singh, Electrocatalytic properties of new active ternary ferrite film anodes for O2 evolution in alkaline medium, Electrochim. Acta 47 (2002) 3873–3879. https://doi.org/10.1016/S0013-4686(02)00354-7.

[42] F. Švegl, B. Orel, I. Grabec-Švegl, V. Kaučič, Characterization of spinel Co3O4 and Li-doped Co3O4 thin film electrocatalysts prepared by the sol-gel route, Electrochim. Acta 45 (2000) 4359–4371. https://doi.org/10.1016/S0013-4686(00)00543-0.

[43] R.N. Singh, J.F. Koenig, G. Poillerat, P. Chartier, Thin films of CO3O4 and NiCo2O4 prepared by the method of chemical spray pyrolysis for electrocatalysis. Part IV. The electrocatalysis of oxygen reduction, J. Electroanal. Chem. 314 (1991) 241–257.

https://doi.org/10.1016/0022-0728(91)85440-Z.

[44] L.I. Krishtalik, Kinetics and mechanism of anodic chlorine and oxygen evolution reactions on transition metal oxide electrodes, Electrochim. Acta 26 (1981) 329–337. https://doi.org/10.1016/0013-4686(81)85019-0.

[45] J.O.M. Bockris, T. Otagawa, Mechanism of oxygen evolution on perovskites, J. Phys. Chem. 87 (1983) 2960–2971. https://doi.org/10.1021/j100238a048.

[46] R.N. Singh, J.F. Koenig, G. Poillerat, P. Chartier, Thin films of CO3O4 and NiCo2O4 prepared by the method of chemical spray pyrolysis for electrocatalysis. Part IV. The electrocatalysis of oxygen reduction, J. Electroanal. Chem. 314 (1991) 241–257. https://doi.org/10.1016/0022-0728(91)85440-Z.

[47] K.J. Lee, N. Elgrishi, B. Kandemir, J.L. Dempsey, Electrochemical and spectroscopic methods for evaluating molecular electrocatalysts, Nat. Rev. Chem. 1 (2017). https://doi.org/10.1038/s41570-017-0039.

[48] H. Mashiko, K. Yoshimatsu, T. Oshima, A. Ohtomo, Fabrication and Characterization of Semiconductor Photoelectrodes with Orientation-Controlled α-Fe2O3 Thin Films, J. Phys. Chem. C 120 (2016) 2747–2752. https://doi.org/10.1021/ACS.JPCC.5B10838.